

Jing LIU
Yajun XU
Linfeng WANG
Zidan XU
Changke TANG

INFLUENCE OF THE LOCAL DEFECT DISTRIBUTION ON VIBRATION CHARACTERISTICS OF BALL BEARINGS

WPŁYW ROZKŁADU WAD LOKALNYCH NA CHARAKTERYSTYKĘ DRGAŃ ŁOŻYSK KULKOWYCH

Local defects in ball bearings may occur at the center line of raceway and its surrounding areas. However, most current studies were concentrated in studying the influence of the local defect located at the centerline of raceway on the bearing vibrations, where the effects of local defects surround the centerline were ignored. To overcome this problem, based on Hertzian point contact theory and multi-body dynamic algorithm, a multi-body dynamic model considering the offset and angular distributions for a ball bearing with a local defect on its outer raceway is established. The influences of offset distance and skew angle between the geometric center of local defect and the centerline of outer raceway on the bearing vibrations are investigated. The relationship between the offset distance and the impulse waveform characteristics is obtained, as well as that between the skew angle and the impulse waveform characteristics. The results show that the offset distance and skew angle of the local defect have a great influence on the time-domain impulse waveform characteristics of the bearing accelerations. This paper can provide a useful guidance for the accurate diagnosis of early local fault in the ball bearings.

Keywords: ball bearing; local defect; multi-body dynamics; vibrations; distribution.

Wady lokalne łożysk kulkowych mogą występować na linii środkowej bieżni oraz w otaczających ją obszarach. Jednak większość dotychczasowych badań nad wpływem wad lokalnych na drgania łożyska koncentruje się na wadach linii środkowej bieżni ignorując oddziaływanie wad zlokalizowanych w obszarach otaczających tę linię. Aby rozwiązać ten problem, w przedstawionej pracy wykorzystano teorię kontaktu Hertza oraz algorytm do analizy dynamiki układów wieloczłonowych, co pozwoliło na utworzenie modelu dynamiki układu wieloczłonowego uwzględniającego przesunięcie i rozkłady kątowe łożyska kulkowego z lokalną wadą na bieżni zewnętrznej. Badano wpływ wartości przesunięcia i kąta nachylenia między geometrycznym środkiem wady lokalnej a linią środkową bieżni zewnętrznej na drgania łożyska. Otrzymano zależności pomiędzy wartością przesunięcia a charakterystyką przebiegu impulsu, a także między kątem nachylenia a charakterystyką przebiegu impulsu. Wyniki pokazują, że wartość przesunięcia i kąt nachylenia wady lokalnej mają duży wpływ na przebieg przyspieszeń łożyska w dziedzinie czasu. Praca dostarcza użytecznych wskazówek na temat trafnego diagnozowania lokalnych uszkodzeń łożysk kulkowych w ich wczesnych stadiach.

Słowa kluczowe: łożysko kulkowe; wada lokalna; dynamika układów wieloczłonowych; drgania; rozkład.

1. Introduction

Ball bearing plays an important role in mechanical transmission. Nevertheless, localized defects such as crack, spalling and pitting are easily arisen on the raceways when bearings are working under poor conditions, and these events can severely influence the performance of industry machinery [4, 12, 32]. Thus, to reduce the possibility of machineries damages caused by the local defects in the bearings, the precise recognition of the early defects is very important [27, 29]. Investigations of the relationship between local defect and bearing vibrations can provide a useful reference for the accurate identification of early local defect in the bearings [5-7, 13, 30, 31].

Many modelling methods were published to study the vibration features of defective ball bearings. For example, Arslan and Aktürk [1], Sassi et al. [25], Babu et al. [2], Behzad et al. [3], Rafsanjani et al. [24], Patel et al. [23], Liu et al. [14-18], Kankar et al. [8], and Leturiondo et al. [11] proposed kinds of dynamic models of defective ball bearings by considering the defect as the time dependent dis-

placement excitations to study the effects of the defects on the bearing vibrations. Liu et al. [16] introduced a dynamic model of rigid rotor bearing systems to investigate the effects of defect sizes on the vibrations of the system. Khanam et al. [9, 10] and Liu et al. [19] conducted new methods to formulate the defect effects as the time dependent force excitations to study the effects of the local defects on the vibrations of ball bearings and rotor-ball bearing system. Niu et al. [22] developed a novel dynamic model considering the relative slippage and cage effects to analyze the effect of local defect on the ball passing frequencies (BPFs) of a ball bearing. Li et al. [20] proposed a dynamic model of an angular contact ball bearing to investigate the influences of the defect parameters on the variations of contact angles and load distributions of the ball bearing. In the listed literatures, the defects centerlines were all assumed to be parallel with the raceway centerlines. However, observing the practical cases of the ball bearing failure [26], the defect centerline may not be parallel with the raceway centerline, as showed in Fig. 1, which was ignored by the

listed modeling methods. Thus, this paper is focused on developing a multi-dynamic model of a ball bearing with the parallel, offset, and bias local defects.

Before developing a multi-body dynamic model considering the offset and angular distributions for a defective ball bearing, the multi-body algorithm and Hertzian contact theory are introduced in Section 1. Section 2 details the defective ball bearing dynamic model. The layout of the experimental apparatus is discussed and the model validation is detailed in Section 3. The relationship between the offset distance and the impulse waveform characteristics is obtained in Section 4. Conclusions are drawn in Section 5.

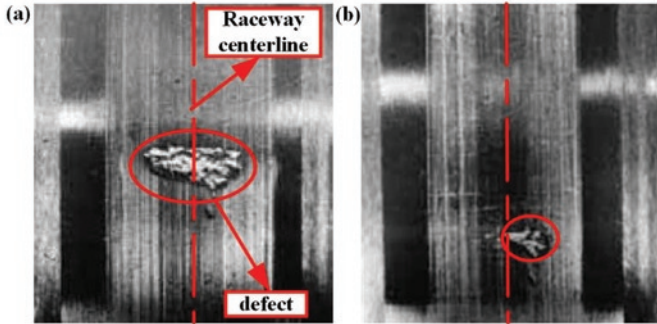


Fig. 1. Schematics of different defect distribution cases. (a) A parallel case and (b) a bias case. [26]

2. Calculation methods of the contact force and stiffness

2.1. Calculation method of the contact force

In the multi-body dynamic model of the ball bearing, an explicit contour recognition method is utilized for the contact detection between the ball and raceways. As illustrated in Fig. 2, an example of sphere-to-flat contact model is used to describe the calculation method of contact force in the simulation model. In Fig. 2, I and J are the undeformed points of sphere and flat bodies, respectively.

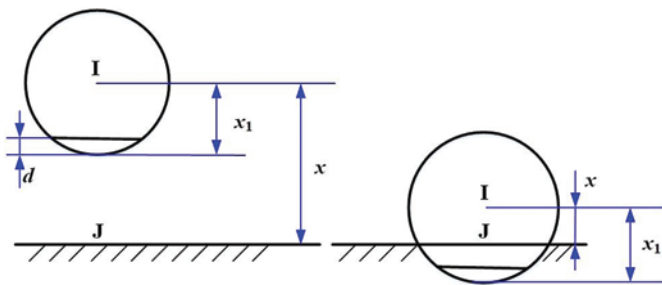


Fig. 2. The calculation method of contact force in the simulation model

The contact force between a sphere and a flat surface is calculated as [21]:

$$F = \begin{cases} 0 & x > x_1 \\ F_e - F_c & x < x_1 \end{cases} \quad (1)$$

where F is the contact force; F_e is the elastic force; F_c is the damping force; x is the distance variable used to compute an impact function; and x_1 is the free length of x (if x is less than x_1 , a positive value for the force is used). The equations of F_e and F_c are represented as [21]:

$$F_e = K_c(x - x_1)^e \quad (2)$$

$$F_c = \text{STEP}(x, x_1 - d, c_{\max}, x_1, 0) \times \dot{x} \quad (3)$$

where K_c is the stiffness of the boundary surface interaction; d is the boundary penetration; e is the exponent of the force deformation characteristic, which is usually set as 1.5 for the steel bodies; c_{\max} is the maximum damping coefficient, which is set as 350 N s/m ; The damping of the ball bearing is typically in the order of $0.25\text{-}2.5 \times 10^{-5}$ times the linearized stiffness of the bearing [16]. The damping coefficient c_{\max} in Eq. (3) is obtained within this range and \dot{x} is the first-order time derivative of x . As depicted in Fig. 3, the STEP function in Eq. (3) represents that the damping coefficient value decreases from c_{\max} to 0 when x increases from $x_1 - d$ to x_1 .

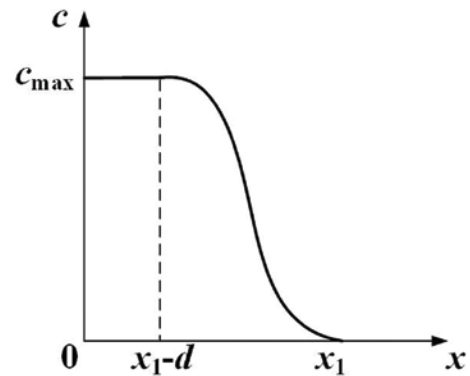


Fig. 3. A STEP function

2.2. Calculation method of contact stiffness

As depicted in Fig. 4, an inner race-to-ball contact model is used to describe the point-contact between raceways and balls. Q is the external force applied on the ball.

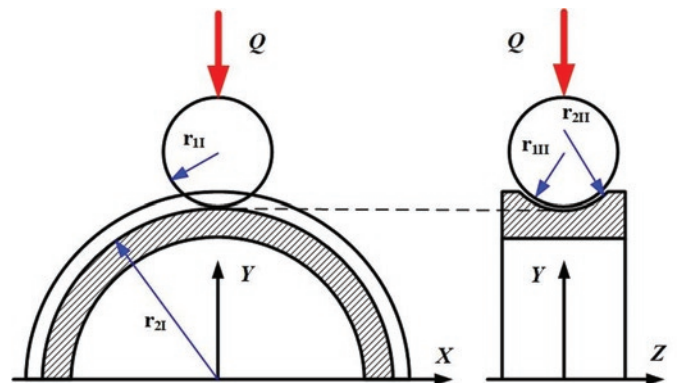


Fig. 4. Schematic of Hertzian point contact

Base on Hertzian point-contact theory, the contact stiffness between inner race and ball is represented as [28]:

$$K_c = \frac{1}{\sqrt{e_s^3 (\sum \rho)}} \quad (4)$$

where K_c is the contact stiffness between inner race and ball. $\sum \rho$ and e_s are, separately, the sum of principle curvatures and an intermediate variable related to K and μ , represented as:

$$\sum \rho = \rho_{1I} + \rho_{1II} + \rho_{2I} + \rho_{2II} = \frac{1}{r_{1I}} + \frac{1}{r_{1II}} + \frac{1}{r_{2I}} + \frac{1}{r_{2II}} \quad (5)$$

$$e_\delta = 2.7910 \times 10^{-4} \frac{2K}{\pi\mu} \quad (6)$$

where ρ_{1I} , ρ_{1II} , ρ_{2I} and ρ_{2II} are principle curvatures of the ball and inner race, equal to the reverse of radius r_{1I} , r_{1II} , r_{2I} and r_{2II} , subscripts I and 2 are representing the ball and inner race, subscripts I and II representing two mutually perpendicular principal planes; K is the first order elliptic integral; μ is a coefficient relates to the dimension of contact region between the ball and inner race. K and μ are separately represented as:

$$K = \int_0^{\pi/2} \frac{1}{\sqrt{1-k^2 \sin^2 \phi}} d\phi \quad (7)$$

$$\mu = 3 \sqrt{\frac{1}{1-k^2} \times \frac{2E}{\pi}} \quad (8)$$

where k is an intermediate variable with no meaning. There is a correlation between K and $F(\rho)$ can be represented as:

$$F(\rho) = \frac{(2-k^2)E - 2(1-k^2)K}{k^2 E} \quad (9)$$

where E and $F(\rho)$ are the second order elliptic integral and instrumental variable related to the dimension of ball and inner race, separately, represented as:

$$E = \int_0^{\pi/2} \sqrt{1-k^2 \sin^2 \phi} d\phi \quad (10)$$

$$F(\rho) = \frac{|\rho_{1I} - \rho_{1II}| + |\rho_{2I} - \rho_{2II}|}{\sum \rho} \quad (11)$$

3. Dynamic modelling of a defective ball bearing

The multi-body deep groove ball bearing model has the same geometric parameters of 6308-2RZ ball bearing, the parameter values of the model are plotted in Table. 1. To model such defective ball bearing, MSC. Adams is used here. In this model, a point motion is applied on the mass center of inner ring, and the inner ring is connected with ground by a planar joint in order to limit the inner ring to rotate through the centroid axis while moving in the working plane. The spring damper system is used to connect the inner ring and ground both in the horizontal and vertical directions in order to model the structural stiffness and damping of the driving shaft. The cage can rotate around the mass center of inner race to accommodate the balls at a certain angular spacing. The bushing is used to connect the outer ring with ground in order to model the structural stiffness and damping of the bearing mount and limit the rotational degree of the outer ring around the centroid axis. Contact constraints are defined between each ball and the cage, inner ring and outer ring. The schematic of the multi-body dynamic model is depicted in Fig. 5.

In this multi-body dynamic model, the defect is modeled as rectangular shape in the outer raceway by removing a section. The mod-

Table 1. Parameters of 6308-2RZ bearing

Parameter	Value
Inner ring diameter (d_i)/mm	40
Outer ring diameter (D)/mm	90
Ball diameter (D_b)/mm	15.081
Pitch diameter (d_m)/mm	65
Width (C)/mm	23
Number of Balls (Z)	8

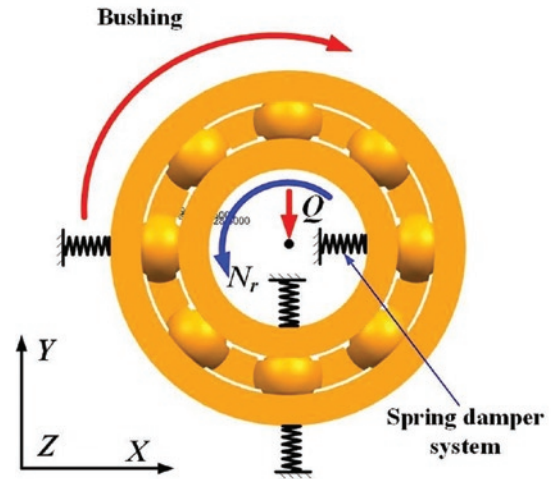


Fig. 5. Schematic of multi-body dynamic model



Fig. 6. Models of healthy outer raceway and outer raceway with local defect

els of the healthy and defective outer raceway are illustrated in Fig. 6, where B and L are, separately, the defect length and width.

4. Experimental validation

As depicted in Fig. 7, to validate the multi-body dynamic model of a ball bearing with a localized defect on the outer ring, an experiment is applied. The test bearing is placed on the non-driving end of the shaft. A defect with $L=1$ mm and $B=23$ mm are introduced on the outer ring of test bearing using a wire-electrode cutting method as shown in Fig. 7(b). The shaft rotates at the speed of 1800 r/min. A radial load of 150 N is applied on the outer ring along the Y -direction. The data collection system consists of an accelerometer with a sensitivity of 9.91 mV/g, a LMS data collection system, and a computer. The accelerometer is mounted on the outer ring of test bearing to measure the vibrations. The signals are obtained at a sampling frequency of 20 kHz and a sampling time of 10 s.

The pulse waveforms of acceleration of outer ring obtained from simulation and experiment results of healthy bearing are compared, as shown in Fig. 8. Both the amplitudes of simulation and experiment

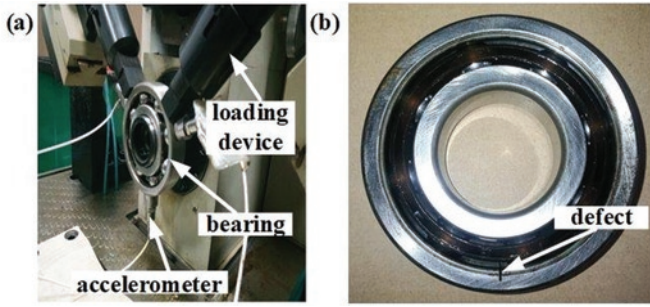


Fig. 7. (a) An experiment setup and (b) the test bearing with a defect on the outer ring

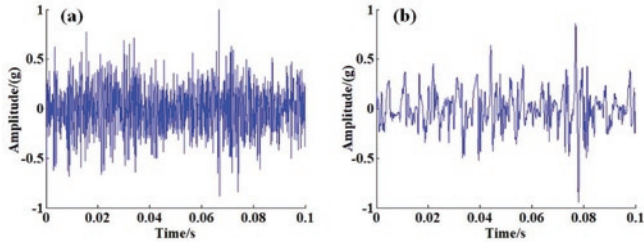


Fig. 8. Comparisons of pulse waveforms of the accelerations along Y direction from the experiment and simulation. (a) Experimental result of the healthy ball bearing, and (b) simulation result of the healthy ball bearing

pulse waveforms are approximate ± 1 g, and a great cohesion between the two pulse waveforms are observed.

For further validation, the frequency spectra of accelerations of the outer ring obtained from the simulation and experiment results of the healthy bearing are compared, as shown in Fig. 9. There is small difference between the shaft rotation frequencies ($f_i = N_r / 60$) obtained from experiment (29.69 Hz) and simulation (27.96 Hz), which can be caused by some difference in the motor speed. Some differences between the ball passing frequencies of the inner ring (BPFIs = $Zf_i / (2(1 - D_b / d_m))$) obtained from experiment (151.6 Hz) and simulation (149.7 Hz), and between the ball passing frequencies of the outer ring (BPFOs = $Zf_i / (2(1 + D_b / d_m))$) obtained from experiment (95.31 Hz) and simulation (91.99 Hz) are observed, they may be caused by some slipping and skidding between the balls and races.

The pulse waveforms of acceleration of the outer ring obtained from simulation and experiment results of defective bearing are compared, as shown in Fig. 10. Both the amplitudes of simulation and experiment pulse waveforms are approximate ± 60 g, and the excitation

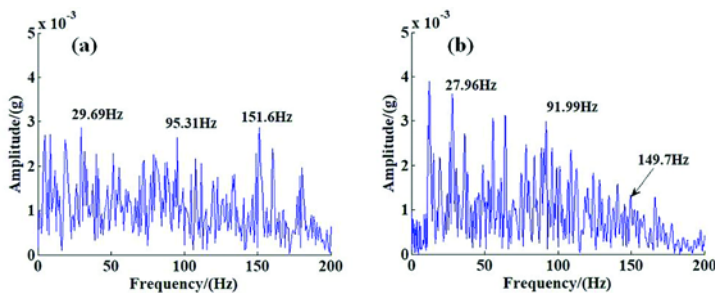


Fig. 9. Comparisons of frequency spectra of the accelerations along Y direction from the experiment and simulation. (a) Experimental result of the healthy ball bearing, and (b) simulation result of the healthy ball bearing

periods of experiment and simulation pulse waveforms are 0.01083 s and 0.01084 s, separately.

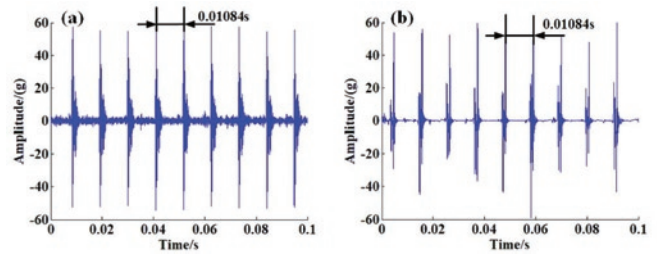


Fig. 10. Comparisons of pulse waveforms of the accelerations along Y direction from the experiment and simulation. (a) Experimental result of the defective ball bearing, and (b) simulation result of the defective ball bearing

For further validation, the frequency spectra of accelerations of the outer ring obtained from simulation and experiment results of defective bearing are compared, as shown in Fig. 9. There is small difference between the shaft rotation frequencies obtained from experiment (29.69 Hz) and simulation (30.53 Hz). Some differences between the BPFIs obtained from experiment (150 Hz) and simulation (146 Hz), and between the BPFOs obtained from experiment (92.19 Hz) and simulation (91.93 Hz). Both the experiment and simulation results of healthy and defective ball bearings show great cohesions with each other, then the multi-body dynamic model is validated.

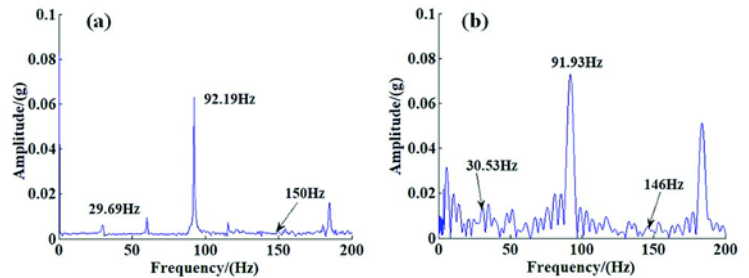


Fig. 11. Comparisons of frequency spectra of the accelerations along Y direction from the experiment and simulation. (a) Experimental result of the defective ball bearing, and (b) simulation result of the defective ball bearing

Table 2. Comparisons of frequencies of healthy and defective bearings from simulation

Frequencies	Healthy bearing	Defective bearing	Difference (%)
f_i	27.96	30.53z	8.42
BPFO	91.99	91.93	0.06
BPFI	149.7	146	2.53

There are small differences between the shaft rotation frequencies (8.42%), the BPFIs (0.06%) and the BPFOs (2.53%) of healthy and defective bearing obtained from simulation, as shown in Table. 2, they may be caused by some slipping and skidding between the balls and races.

5. Results discussions

In the multi-body dynamic model, the inner ring rotates at the speed of $N_r=1800$ r/min and a radial load of $Q=480$ N is applied on the inner ring along the Y-direction. The effects of defect sizes and locations on the vibrations of the ball bearing are studied. Then, the pulse waveforms of the accelerations and

displacements of outer ring along Y direction are compared to investigate the influences of offset distance and skew angle to the vibrations of the bearing.

5.1. Effects of the defect sizes

To study the relationship between the defect size and the vibration of bearing, three different sizes of local defects are introduced on the outer ring, as shown in Fig. 12. The defects are numbered from left to right as O1, O2 and O3, L_1, L_2 and L_3 are three different lengths, their values are plotted in Table 3.

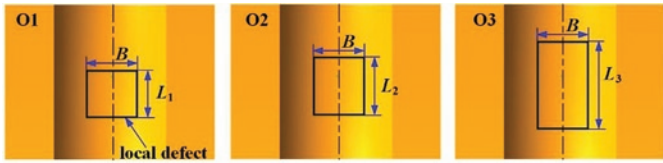


Fig. 12. Outer ring model with three different sizes of local defect

Table 3. Sizes of local defects

Number	Width (B)/mm	Length (L)/mm
O1 ($B \times L_1$)	1	1
O2 ($B \times L_2$)	1	3
O3 ($B \times L_3$)	1	6

The displacement results of the outer ring are shown in Fig. 13, the excitations are clearly observed when the ball passes through the local defect. When the ball passes through defects O1, O2 and O3, the excitation durations of pulse waveforms are T_1, T_2 and T_3 , and a relationship of $T_1 < T_2 < T_3$ can be observed. Moreover, with the increment of defect sizes, the amplitudes of the pulse waveforms increase. Then the model has achieved a good transient response when the ball passes through the local defect.

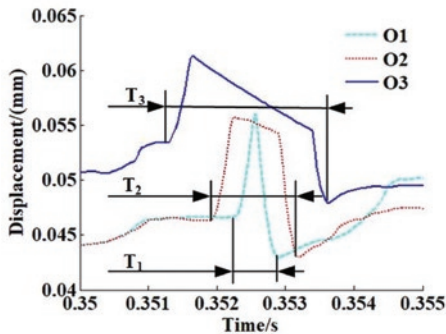


Fig. 13. The pulse waveforms of displacements of the outer ring for different defect sizes

5.2. Effect of the offset distance

In order to investigate the effects of offset distance to the outer ring vibration, O1 defect with three different offset distances $H=0$ mm, $B/3$ mm and $B/2$ mm are introduced to the outer ring, as depicted in Fig. 14. Using the model, some displacement and acceleration results of the outer ring are obtained.

When the ball passes through the offset defects, the excitations caused by the defects are clearly observed. The pulse waveforms of the defective outer ring with different offset distances are shown in Fig. 15. For the case of $H=0$ mm, the excitation amplitudes of displacement and acceleration are 0.0585mm and 28.82 g, separately.

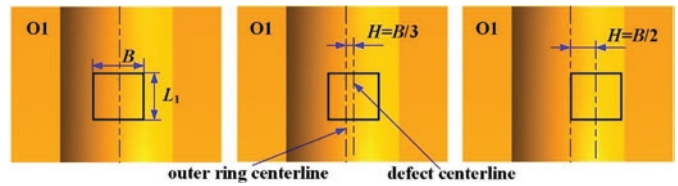


Fig. 14. Defective outer ring models of three different offset distances

For the case of $H=B/3$ mm, the excitation amplitudes of displacement and acceleration are 0.05695 mm and 22.48 g, separately. For the case of $H=B/2$ mm, the excitation amplitudes of displacement and acceleration are 0.05545 mm and 15.64 g, separately. The results show that the amplitudes of excitations are greatly affected by the offset distance of defects. Note that the amplitudes of excitations decrease with the increment of offset distance. This is due to the fact that with the offset distance increase, the maximum depth of the ball falls into

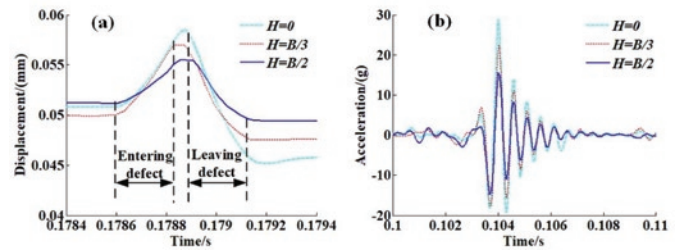


Fig. 15. The pulse waveforms of the defective outer ring with different offset distances. (a) Displacements, and (b) accelerations

the defect decrease correspondingly.

5.3. Effect of the bias angle

For the study of the relationship between bias angle and outer ring vibration, O2 defect with three different bias angles $\theta=0$ degree, 30 degree and 60 degree are introduced to the outer ring, as depicted in Fig. 16. Using the model, displacement and acceleration results of the

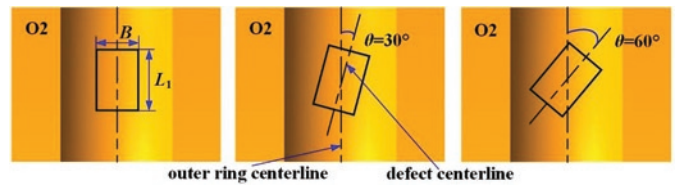


Fig. 16. Defective outer ring models of three different skew angles

outer ring are obtained.

The pulse waveforms of the defective outer ring with different bias angles are shown in Fig. 17, where T_1, T_2 and T_3 represent the excitation durations for the cases of $\theta=0$ degree, 30 degree and 60 degree, separately. The relationship of $T_1 > T_2 > T_3$ can be clearly observed, indicate that the excitation duration decreases with the increment of bias angle. This is due to the fact that with the bias angle increase, the angle distance of defect along outer ring centerline decrease correspondingly. The curve sections $j_2-k_2-l_2$ and $j_3-k_3-l_3$ depict the continuous excitations caused by local defect for the cases of $\theta=30$ degree and 60, separately. Differently, the curve section $j_1-k_1-l_1-m_1$ that for the case of $\theta=0$ degree has an extra relatively flat section k_1-l_1 , this is because during this period the ball continuously contact with the length edges of local defect, then no sudden impact happened for the outer ring. Moreover, the excitation amplitudes of acceleration for the cases of $\theta=30$ degree and 60 degree are great than that for the case of $\theta=0$ degree. The result shows that the excitation amplitudes of acceleration increase with the increment of bias angle.

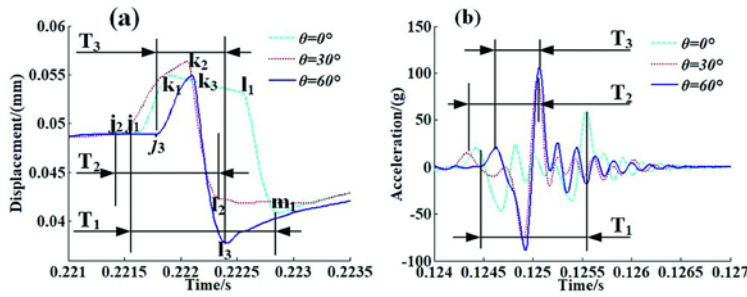


Fig. 17. The pulse waveforms of the defective outer ring with different skew angles. (a) Displacements, and (b) accelerations

5.4. Effect of the inner ring speed

In order to investigate the effects of inner ring speed to the outer ring vibration, the pulse waveforms of the defective outer ring with O3 defect under three different inner ring speed conditions $N_r = 900$ r/min, 1800 r/min and 3600 r/min are compared, as shown in Fig. 18. T_1 , T_2 and T_3 represent the excitation durations for the cases of $N_r = 900$ r/min, 1800 r/min and 3600 r/min, separately. The relationship of $T_1 > T_2 > T_3$ can be clearly observed, indicate that the excitation decreases

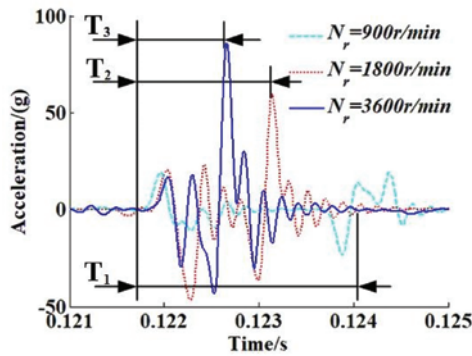


Fig. 18. The pulse waveforms of the defective outer ring under three different speed conditions

Nomenclature

B	Defect width, mm	K	The first order elliptic integral
c_{max}	Maximum damping coefficient, N/(m/s)	K_c	Contact stiffness between inner race and ball, N/mm
C	Bearing width, mm	L	Defect length, mm
d	Boundary penetration at which the Adams solver applies full damping, mm	Q	External force applied on the ball, N
d_i	Inner ring diameter, mm	r_{1I}	Principle radius of the ball in plane I, mm
d_m	Pitch diameter, mm	r_{1II}	Principle radius of the ball in plane II, mm
D	Outer ring diameter, mm	r_{2I}	Principle radius of inner ring in plane I, mm
D_b	Ball diameter, mm	r_{2II}	Principle radius of inner ring in plane II, mm
e_δ	An intermediate variable related to K and μ	x	Distance variable used to compute an impact function, mm
E	The second order elliptic integral	x_1	Free length of x , mm
f_i	Rotational frequency of inner ring, Hz	Z	Number of Balls
BPFO	Ball passing frequency of outer ring, Hz	ρ_{1I}	Principle curvature of the ball in plane I, mm^{-1}
BPMF	Ball passing frequency of inner ring, Hz	ρ_{1II}	Principle curvature of the ball in plane II, mm^{-1}
F	Contact force, N		

with the increment of inner ring speed. Moreover, the excitation amplitude increases with the growth of inner ring speed.

6. Conclusion

A multi-body dynamic model is presented to consider the effects of the offset and bias defects. The contact stiffness is calculated by Hertzian contact theory. The effects of sizes, offset distance and bias angle of the rectangular shape defect on the vibrations of ball bearing are analyzed. The obtained results show that the given method can provide a more accurate and reasonable analytical method for studying the vibrations of ball bearing with a local offset defect. Some conclusions are listed as follows:

- (1) The amplitudes of pulse waveforms caused by defect increase with the increment of defect sizes.
- (2) The amplitudes of excitations are greatly affected by the offset distance of defects. Note that the amplitudes of excitations decrease with the increment of offset distance. The reason is that with the offset distance increase, the maximum depth of the ball falls into the defect decrease correspondingly.
- (3) The excitation duration decreases with the increment of bias angle. This is due to the fact that with the bias angle increase, the angle distance of defect along outer ring centerline decrease correspondingly. Moreover, the excitation amplitudes of acceleration increase with the increment of bias angle.
- (4) The excitation decreases with the increment of inner ring speed and the excitation amplitude increase with the growth of inner ring speed.

Acknowledgments

The authors are grateful for the National Natural Science Foundation of China (No. 51605051), Chongqing Research Program of Basic Research and Frontier Technology (No. cstc2017jcyjAX0202), and Chongqing Special Key R & D Projects for Technology Innovation of Key Industries (No. cstc2017zdcy-zdyfX0101).

F_e	Elastic force, N	ρ_{21}	Principle curvature of inner ring in plane I, mm^{-1}
F_c	Damping force, N	ρ_{11}	Principle curvature of the ball in plane I, mm^{-1}
$F(\rho)$	Instrumental variable related to the dimension of ball and inner race	ρ_{211}	Principle curvature of inner ring in plane II, mm^{-1}
k	An intermediate variable with no meaning	μ	Coefficient relates to the dimension of contact region between the ball and inner race

References

1. Arslan H., Aktürk N. -An investigation of rolling element vibrations caused by local defects. *Journal of Tribology* 2008; 130(4): 041101, <https://doi.org/10.1115/1.2958070>.
2. Babu C. K., Tandon N., Pandey R. K. -Nonlinear vibration analysis of an elastic rotor supported on angular contact ball bearings considering six degrees of freedom and waviness on balls and races. *Journal of Vibration and Acoustics* 2014; 136(4): 044503, <https://doi.org/10.1115/1.4027712>.
3. Behzad M., Bastami A. R., Mba D. -A new model for estimating vibrations generated in the defective rolling element bearings. *Journal of Vibration and Acoustics* 2011; 133(4): 041011, <https://doi.org/10.1115/1.4003595>.
4. Chen Z., Zhai W., Wang K. -Vibration feature evolution of locomotive with tooth root crack propagation of gear transmission system. *Mechanical Systems and Signal Processing* 2019; 115: 29-44. <https://doi.org/10.1016/j.ymssp.2018.05.038>
5. Cui L., Huang J., Zhang F., Chu F. -HVSRRMS localization formula and localization law: Localization diagnosis of a ball bearing outer ring fault, *Mechanical Systems and Signal Processing* 2019; 120(1): 608-629, <https://doi.org/10.1016/j.ymssp.2018.09.043>.
6. Cui L., Wang X., Xu Y., Jiang H., Zhou J. -A novel Switching Unscented Kalman Filter method for remaining useful life prediction of rolling bearing, *Measurement* 2019; 135: 678-684. <https://doi.org/10.1016/j.measurement.2018.12.028>
7. Cui L., Wang J., Seungchul L. -Matching Pursuit of an Adaptive Impulse Dictionary for Bearing Fault Diagnosis. *Journal of Sound and Vibration* 2014; 333(10): 2840-2862. <https://doi.org/10.1016/j.jsv.2013.12.029>
8. Kankar P. K., Sharma S. C., Harsha S. P. -Vibration based performance prediction of ball bearings caused by localized defects. *Nonlinear Dynamics* 2012; 69(3): 847-875, <https://doi.org/10.1007/s11071-011-0309-7>.
9. Khanam S., Dutt J. K., Tandon N. -Impact force based model for bearing local fault identification. *Journal of Vibration and Acoustics* 2015; 137(5): 051002, <https://doi.org/10.1115/1.4029988>.
10. Khanam S., Tandon N., Dutt J. K. -Multi-event excitation force model for inner race defect in a rolling element bearing. *Journal of Tribology* 2016; 138(1): 011106, <https://doi.org/10.1115/1.4031394>.
11. Leturiondo U., Salgado O., Galar D. -Multi-body modelling of rolling element bearings and performance evaluation with localised damage. *Eksplotacja i Niezawodność – Maintenance and Reliability* 2016; 18(4): 638-648, <https://doi.org/10.17531/ein.2016.4.20>.
12. Liu J., Shao Y. -Overview of dynamic modelling and analysis of rolling element bearings with localized and distributed faults. *Nonlinear Dynamics* 2018; 93 (4): 1765-1798, <https://doi.org/10.1007/s11071-018-4314-y>.
13. Liu J., Shao Y. -An improved analytical model for a lubricated roller bearing including a localized defect with different edge shapes. *Journal of Vibration and Control* 2018; 24(17): 3894-3907, <https://doi.org/10.1007/s11071-017-3571-5>.
14. Liu J., Shao Y., Lim T. C. -Vibration analysis of ball bearings with a localized defect applying piecewise response function. *Mechanism and Machine Theory* 2012; 56: 156-169, <https://doi.org/10.1016/j.mechmachtheory.2012.05.008>.
15. Liu J., Shi Z., Shao Y. -An investigation of a detection method for a subsurface crack in the outer race of a cylindrical roller bearing. *Eksplotacja i Niezawodność – Maintenance and Reliability* 2017; 19(2): 211-219, <https://doi.org/10.17531/ein.2017.2.8>.
16. Liu J., Shao Y. Dynamic modeling for rigid rotor bearing systems with a localized defect considering additional deformations at the sharp edges. *Journal of Sound and Vibration* 2017; 398: 84-102, <https://doi.org/10.1016/j.jsv.2017.03.007>.
17. Liu J., Tang C., Shao Y. -An innovative dynamic model for vibration analysis of a flexible roller bearing. *Mechanism and Machine Theory* 2019; 135: 27-39. <https://doi.org/10.1016/j.mechmachtheory.2019.01.027>
18. Liu J., Xu Z., Zhou L., Yu W., Shao Y. -A statistical feature investigation of the spalling propagation assessment for a ball bearing. *Mechanism and Machine Theory* 2019; 131: 336-350. <https://doi.org/10.1016/j.mechmachtheory.2018.10.007>
19. Liu J., Xu Y., Shao Y. -Dynamic modelling of a rotor-bearing-housing system including a localized fault. *Journal of Multi-body Dynamics* 2018; 232(3): 385-397, <https://doi.org/10.1177/1464419317738427>.
20. Li X., Yu K., Ma H., Cao L., Luo Z., Li H., Che, L. -Analysis of varying contact angles and load distributions in defective angular contact ball bearing. *Engineering Failure Analysis* 2018; 91: 449-464, <https://doi.org/10.1016/j.engfailanal.2018.04.050>.
21. MSC. Software. Adams/View help - Adams 2013. America. MSC. Software, 2013.
22. Niu L., Cao H., He Z., Li Y. -A systematic study of ball passing frequencies based on dynamic modeling of rolling ball bearings with localized surface defects. *Journal of Sound and Vibration* 2015; 357: 207-232, <https://doi.org/10.1016/j.jsv.2015.08.002>.
23. Patel V. N., Tandon N., Pandey R. K. -A dynamic model for vibration studies of deep groove ball bearings considering single and multiple defects in races. *Journal of Tribology* 2010; 132(4): 041101, <https://doi.org/10.1115/1.4002333>.
24. Rafsanjani A., Abbasion S., Farshidianfar A., Moeenfar, H. -Nonlinear dynamic modeling of surface defects in rolling element bearing systems. *Journal of Sound and Vibration* 2009; 319(3): 1150-1174, <https://doi.org/10.1016/j.jsv.2008.06.043>.
25. Sassi S., Badri B., Thomas M. -A numerical model to predict damaged bearing vibrations. *Journal of Vibration and Control* 2007; 13(11): 1603-1628. <https://doi.org/10.1177/1077546307080040>.
26. SKF. Bearing failures and their causes. Sweden. Palmeblads Tryckeri AB, 1994.
27. Song L., Wang H., Chen P. -Vibration-Based Intelligent Fault Diagnosis for Roller Bearings in Low-Speed Rotating Machinery. *IEEE TRANSACTIONS ON INSTRUMENTATION AND MEASUREMENT* 2018; 67(8): 1887-1899. <https://doi.org/10.1109/TIM.2018.2806984>

28. T. A. Harris, M. N. Kotzalas, *Essential Concepts of Bearing Technology*. 5th Ed. Beijing: China Machine Press, 2006.
29. Wang H., Li S., Song L., Cui L. -A novel convolutional neural network based fault recognition method via image fusion of multi-vibration-signals, *Computers in Industry* 2019; 105: 182-190. <https://doi.org/10.1016/j.compind.2018.12.013>
30. Wang Y., Xu G., Luo A., Liang L., Jiang K. -An online tacholeless order tracking technique based on generalized demodulation for rolling bearing fault detection. *Journal of Sound and Vibration* 2016; 367: 233-249, <https://doi.org/10.1016/j.jsv.2015.12.041>.
31. Xi S., Cao H., Chen X., Niu L. -A dynamic modeling approach for spindle bearing system supported by both angular contact ball bearing and floating displacement bearing. *Journal of Manufacturing Science and Engineering* 2017; 140(2), 021014, <https://doi.org/10.1115/1.4038687>.
32. Zhang T., Chen Z., Zhai W. -Establishment and validation of a locomotive-track coupled spatial dynamics model considering dynamic effect of gear transmissions. *Mechanical Systems and Signal Processing* 2019; 119: 328-345. <https://doi.org/10.1016/j.ymsp.2018.09.032>

Jing LIU

State Key Laboratory of Mechanical Transmission, Chongqing University, Chongqing, 400030
College Engineering, Chongqing University, Chongqing, 400030
China

Yajun XU**Linfeng WANG****Zidan XU****Changke TANG**

College Engineering, Chongqing University, Chongqing, 400030
China

E-mails: jliu@cqu.edu.cn, xuyajun18728435636@163.com,
13880193794@163.com, 2463928565@qq.com, ticiki@163.com
